

# New results on the massive star-forming region S106 by BEAR spectro-imagery

B. Noel<sup>1,\*</sup>, C. Joblin<sup>1,\*</sup>, J. P. Maillard<sup>2,\*</sup>, and T. Paumard<sup>2</sup>

<sup>1</sup> Centre d'Étude Spatiale des Rayonnements, CNRS et Université Paul Sabatier, 9 Av. du Colonel Roche,  
31028 Toulouse Cedex 4, France  
e-mail: Christine.Joblin@cesr.fr

<sup>2</sup> Institut d'Astrophysique de Paris, CNRS et Université P. & M. Curie, 98 bis Bd. Arago, 75014 Paris, France  
e-mail: maillard@iap.fr

Received 30 July 2004 / Accepted 20 January 2005

**Abstract.** As a typical example of interaction of a massive star with its parent cloud, the close environment of S106 IR in the star-forming region S106 was observed at high spectral resolution ( $\sim 16 \text{ km s}^{-1}$ ). Integral field spectroscopy with BEAR, an imaging Fourier Transform Spectrometer (FTS), on a field of  $\sim 40''$  in diameter, in the  $\text{H}_2$  1–0  $S(1)$ , 2–1  $S(1)$ ,  $\text{Br}\gamma$ , He I and [Fe III] lines. From the data several maps were obtained: intensity, velocity and linewidth in the  $\text{Br}\gamma$  and the  $\text{H}_2$  1–0  $S(1)$  line, 1–0  $S(1)/2$ –1  $S(1)$  line ratio, and continuum emission at  $2.1 \mu\text{m}$ . From the latter, about twenty low-mass stars were detected with photometry in this band, and an estimate of their mass was made leading to the conclusion that S106 is a site of formation of mainly sub-solar mass stars. The intensity structure of the excited molecular gas  $\text{H}_2$  was found to be clumpy while the velocity is almost uniformly at  $v_{\text{LSR}} \approx 1.5 \text{ km s}^{-1}$  except to the south where the velocity reaches up to  $15 \text{ km s}^{-1}$  in a zone limited by the long edge of a rectangular hole in the emission. The  $\text{H}_2$  line ratio map with values from 1 to 9 implies that UV-absorption and shocks are participating in the excitation process. A PDR model with a temperature of 3700 K for S106 IR was used to retrieve the  $\text{H}_2$  gas density and temperature. The density was found to vary between 1 and  $3.5 \times 10^5 \text{ cm}^{-3}$  with corresponding temperatures between 660 and 1240 K. The study of the linewidth distribution indicates for most of the gas a supersonic turbulence with a mean contribution to the observed profiles of  $\geq 6 \text{ km s}^{-1}$ . Turbulence is likely to be responsible for the observed clumpy structure of the excited gas. Point-like spots with a linewidth as high as  $30 \text{ km s}^{-1}$  in one position are detected, which may be vortices in the molecular gas.

The H II region probed by  $\text{Br}\gamma$  shows a broad range of velocity, from  $-45$  to  $+80 \text{ km s}^{-1}$ , organized in velocity structures that correspond to two pairs of large, bipolar outflows originating from the massive source, not directed along the axis of the H II region. Emission lines of He I and [Fe III] are detected in a bright area to the southwest of S106 IR, with point-like structures suggesting photoevaporating clumps. From the velocity data, a 3-D model of the environment of S106 IR is proposed. S106 is an example of an evolved H II region seen face-on. The central source located at the edge of its parent molecular cloud has carved an expanding cylinder of turbulent, atomic gas of  $\approx 0.1 \text{ pc}$  in radius. This massive object was formed by an accretion disk process. The disk is still present and the bipolar outflows are remnants of the massive star activity. A time scale of 1400 yr is estimated for the most recent event. A thin and quiescent clumpy layer of warm  $\text{H}_2$  marks the transition of the H II region to the molecular cloud. From the data, there are locally no signs of ongoing star formation.

**Key words.** stars: formation – ISM: individual objects: Sh 2-106 – instrumentation: interferometers – H II regions – astrochemistry

## 1. Introduction

The star-forming region Sharpless 106 (Sh 2-106), or simply referred to as S106, is dominated by a unique massive source known as S106 IR (Eiroa et al. 1979) or S106 IRS4 (Gehrz et al. 1982).  $K$ -band imaging by Hodapp & Rayner (1991) clearly shows a low-mass star cluster with a centroid located

about  $30''$  to the northeast of S106 IR, and two extended lobes of ionized gas, aligned approximately in the N-S direction in the plane of the sky. The central star powers a bright, spatially extended  $10' \times 3'$  H II region (Schneider et al. 2003) indicating by such a developed region that S106 IR is near the end of its forming phase. From the detection of H I recombination lines (Garden & Geballe 1986; Persson et al. 1988; Van den Ancker et al. 2000) there is agreement that the star responsible for the ionized region is a massive ( $M > 15 M_{\odot}$ ) pre-main sequence O-type star (Felli et al. 1984). An O8 spectral type is

\* Visiting Astronomer, Canada-France-Hawaii Telescope, operated by the National Research Council of Canada, le Centre National de la Recherche Scientifique de France and the University of Hawaii.

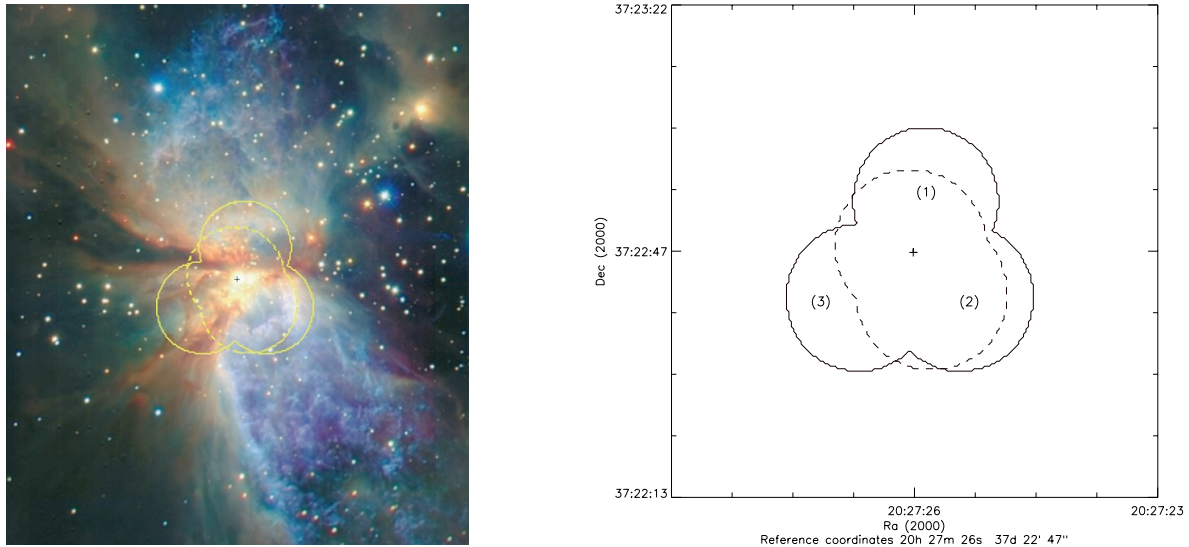


**Fig. 1.** The Br $\gamma$  (dashed) and H $_2$  2.12  $\mu\text{m}$  (solid) fields observed with BEAR. *Left:* superimposed on the composite  $JHK'$  image ( $J$  in blue,  $H$  in green and  $K'$  in red) taken by Oasa (2001). *Right:* the field limits with indication of the field numbers. The cross marks the position of S106 IR.

derived from the detection by the Infrared Space Observatory (ISO) of high-ionization, infrared, ionic lines such as [O III], [Ne III] and [S IV] originating in the surrounding H II region (Van den Ancker et al. 2000). The first evaluation of its distance at 600 pc by Staude et al. (1982) was later revised by Rayner (1994) to a value of  $1.2 \pm 0.2$  kpc which we adopt in this paper. The subsequent derived total luminosity is  $4.2 \times 10^4 L_{\odot}$  (Van den Ancker et al. 2000).

To better study how the massive star is shaping the H II region and disrupting its parent cloud, integral field spectroscopy (IFS) at high spectral and spatial resolution is an ideal tool. At each point of the field the velocity and profile of the emission lines can be determined. It then becomes possible to distinguish velocity structures in the gas and from that to build a model of the kinematics of the stellar environment. Such a study had already been tempted by Solf & Carsenty (1982) but only along a slit, and in the H $\alpha$  line which, because of the high extinction in this region, cannot come from very deep in the cloud. In this paper we present spectro-imagery of the environment of S106 IR obtained at seeing-limited resolution with a spectral resolution of  $\sim 16 \text{ km s}^{-1}$  in Br $\gamma$  (2.16  $\mu\text{m}$ ) and H $_2$  1–0  $S(1)$  (2.12  $\mu\text{m}$ ) and a little more in H $_2$  2–1  $S(1)$  (2.24  $\mu\text{m}$ ). The Br $\gamma$  line makes possible to probe the ionized region. The quadrupolar H $_2$  lines help to study the immediate molecular environment. Mapping in the H $_2$  2.12  $\mu\text{m}$  and the Br $\gamma$  lines was previously obtained by narrow-band imaging (Hayashi et al. 1990). Smith et al. (2001) have presented images in Br $\alpha$  and Bally et al. (1998) in the H $\alpha$  line. All these studies describe only the morphology of the region without making it possible to obtain a good separation between proper emission from the excited gas and the contribution from the continuum emission. The current observations probe the region where the interaction of the massive star with its environment is the most pronounced. The observations are reported in Sect. 2 and the data reduction described in Sect. 3. The analysis of the continuum and the emission line maps are presented in Sect. 4. The excitation conditions in the environment of S106 IR are discussed in Sect. 5 and we conclude with

a 3-D model of the region that incorporates all the velocity information obtained over the field.

## 2. Observations

The central region of S106 was observed in July 1997, July 1998 and October 1999 using BEAR, an imaging FTS installed at the  $f/35$  IR Cassegrain focus of the 3.6 m Canada-France-Hawaii Telescope. Details on the principle and the properties of the instrument are given in Maillard (1995, 2000). The circular field of view has a diameter of 70 pixels, corresponding to 24'' (plate scale of  $\sim 0.35''/\text{pixel}$ ). In order to cover a larger field, three overlapping fields with S106 IR in common were observed with a narrow-band filter ( $2.11 \pm 0.028 \mu\text{m}$ ) containing the H $_2$  1–0  $S(1)$  line. The aim was to acquire the same fields with a Br $\gamma$  filter ( $2.17 \pm 0.029 \mu\text{m}$ ), but only two fields could be recorded. In Fig. 1 the position of the observed fields with their reference number is superimposed on the  $JHK'$  image taken by Oasa (2001) with the CISCO camera at the Subaru telescope, which shows that our observations cover the vicinity of S106 IR. The maximum optical path difference (OPD) of the FTS which was reached, generating cubes of 700 planes, corresponds to a spectral resolution ( $FWHM$ ) of  $16.6 \text{ km s}^{-1}$  for the H $_2$  2.12  $\mu\text{m}$  line and  $16.9 \text{ km s}^{-1}$  for the Br $\gamma$  line. The total integration time of each cube was of the order of 80 min. While fields 1 and 2 in H $_2$  2.12  $\mu\text{m}$  (Fig. 1) were observed in July 1998, field 3 was observed in October 1999. During this last run, S106 was also observed in the H $_2$  2–1  $S(1)$  line ( $2.26 \pm 0.055 \mu\text{m}$  filter) in the three fields of H $_2$  1–0  $S(1)$ . The spectral resolution was  $23.1 \text{ km s}^{-1}$  for fields 1 and 2 and only  $34 \text{ km s}^{-1}$  for field 3.

## 3. Data reduction

The data reduction procedure included two steps: first, the standard production of spectral calibrated cubes from the raw data and second, the building of the continuum intensity map

at  $2.1 \mu\text{m}$  and the velocity structure analysis of the  $\text{H}_2$  1–0  $S(1)$  and  $\text{Br}\gamma$  lines with production of the corresponding maps. A special data reduction procedure was also needed for the construction of the  $\text{H}_2$  1–0/2–1 line ratio map.

### 3.1. BEAR processing

The first step was conducted by using the IDL-written chain of BEAR data reduction programs whose main steps are listed in Maillard (2000). After the basic operations made under the “bearprocess” procedure, further processing includes absolute calibration (A0 standard star HD 162208 for the  $2.17$  and the  $2.12 \mu\text{m}$  filters, HD 1160 for the  $2.26 \mu\text{m}$  filter), spectral re-sampling (sample size of  $\approx 1.2 \text{ km s}^{-1}$  for the line profiles), and cube merging. The final cubes in  $\text{Br}\gamma$  and  $\text{H}_2$   $2.12 \mu\text{m}$  were created by merging the elementary cubes: two for  $\text{Br}\gamma$  and three for  $\text{H}_2$ . The cube merging operation is performed on two overlapping cubes with respect to a common point source, which was here the star S106 IR. The merging sequence was repeated twice for  $\text{H}_2$  1–0  $S(1)$  since three fields had been observed. However, as the last observation had been made in a run 15 months after the first one, the last cube (field 3 in Fig. 1) had to be shifted by 20 planes to match the difference in line velocity. After merging, the cube containing the observations of the  $\text{H}_2$  1–0  $S(1)$  line was  $106 \times 110 \times 769$  pixels in size, the  $\text{Br}\gamma$  line cube  $80 \times 90 \times 769$  pixels. Finally, to increase the signal-to-noise ratio a spatial smoothing with a box of  $3 \times 3$  pixels (approximately  $1''$ ) was operated.

### 3.2. Spectral analysis of the final cubes

To reduce the computing time a preliminary line search program produced a set of field positions where lines had been detected within the spectrum. Then, the detected lines were fitted using Gaussian profiles, and different maps were generated.

#### 3.2.1. Line detection

The useful range of the  $\text{H}_2$  1–0  $S(1)$  and  $\text{Br}\gamma$  filters being narrow ( $\sim 50 \text{ cm}^{-1}$ ), the continuum can be considered as constant in this domain. For each extracted spectrum its mean intensity as well as its rms noise were calculated, estimated over the ranges without the lines under study and the atmospheric OH lines present in the filter ranges. The mean intensity was then subtracted from each spectrum. The position, maximum intensity of the spectrum and signal-to-noise ratio (SNR) at this maximum were recorded. To eliminate the parasitic OH lines, a line profile was saved if its position was within  $100 \text{ km s}^{-1}$  around the rest frequency of the line of interest. For subsequent line fitting a range of  $\pm 100 \text{ km s}^{-1}$  around the line position for  $\text{H}_2$  and  $\pm 150 \text{ km s}^{-1}$  for  $\text{Br}\gamma$  was recorded for the lines of  $\text{SNR} \geq 3$ .

#### 3.2.2. Line fitting

In the case of the  $2.12 \mu\text{m}$   $\text{H}_2$  line the spectral lines previously selected were fitted by a Gaussian profile convolved to the

instrumental lineshape (ILS). For a FTS, this is a sinc function only depending on the maximum OPD. From the fits, maps of integrated line intensity, of velocity expressed in the Local Standard of Rest (LSR) reference frame, and of width of the Gaussian profiles ( $FWHM$ ) were constructed. The pixels at the position of S106 IR were not usable and were removed in all the maps.

The  $\text{Br}\gamma$  line profiles could be clearly seen as being made of several components, indicative of multiple flows. By applying a procedure developed for BEAR data by Paumard et al. (2004), the lines were fitted with a multi-Gaussian profile (up to 3 components). The individual velocity components were then grouped in spatial structures by applying criteria to the velocity gradient between a given pixel and its neighbors, making it possible to build their respective map.

### 3.3. Construction of the $\text{H}_2$ 1–0/2–1 ratio map

The merging procedure (Sect. 3.1) was not applicable in the case of the  $\text{H}_2$  2–1  $S(1)$  line since the three cubes happened to be of different length, because of the lack of observing time. The data analysis described in the previous section was therefore performed on each separate cube. However, due to the larger bandwidth of the filter increasing the photon noise and the weaker emission in the  $\text{H}_2$  2–1 line, this line could be detected only for some pixels of the field. For the other pixels, the  $\text{H}_2$  1–0/2–1 ratio was derived by completing the  $\text{H}_2$  2–1  $S(1)$  integrated intensity map at a maximum level of  $2.5\sigma$  rms. The final ratio map was obtained after merging the three individual 2–1  $S(1)$  intensity maps, centered relative to the  $\text{H}_2$  1–0  $S(1)$  intensity map.

### 3.4. Star detection

A continuum map at  $\approx 2.1 \mu\text{m}$  (Fig. 2) was generated from the cubes of the  $\text{H}_2$  1–0  $S(1)$  line filter by integrating all the planes in the filter bandpass out of the emission lines (atmospheric OH and  $\text{H}_2$  lines). This map was used to search for stellar sources. In standard  $K$ -band imaging the large amount of diffuse light from the massive star together with nebular emission make the detection of stars difficult in the central region. Hence, Hodapp & Rayner (1991) detected young stars only outside the nebula. With the  $2.1 \mu\text{m}$  map the continuum of a star is seen against only a narrow range of the diffused light emission, and without any contribution of emission lines. This residual continuum can be subtracted from the flux measurement of a star continuum providing accurate photometry. The IDL package *Starfinder* (Diolaiti et al. 2000)<sup>1</sup> was used on this map with a point spread function (PSF) derived from an average of the four brightest stars (excluding S106 IR). Then, a new PSF was averaged over all the detected stars, and the procedure was repeated. The detected stars, finally, have a SNR at the peak better than 6.4, and the correlation with the PSF is always better than 80%. From the integrated flux the magnitude of the sources estimated at  $2.1 \mu\text{m}$  was derived.

<sup>1</sup> <http://boas5.bo.astro.it/~giangi/StarFinder/paper6.htm>

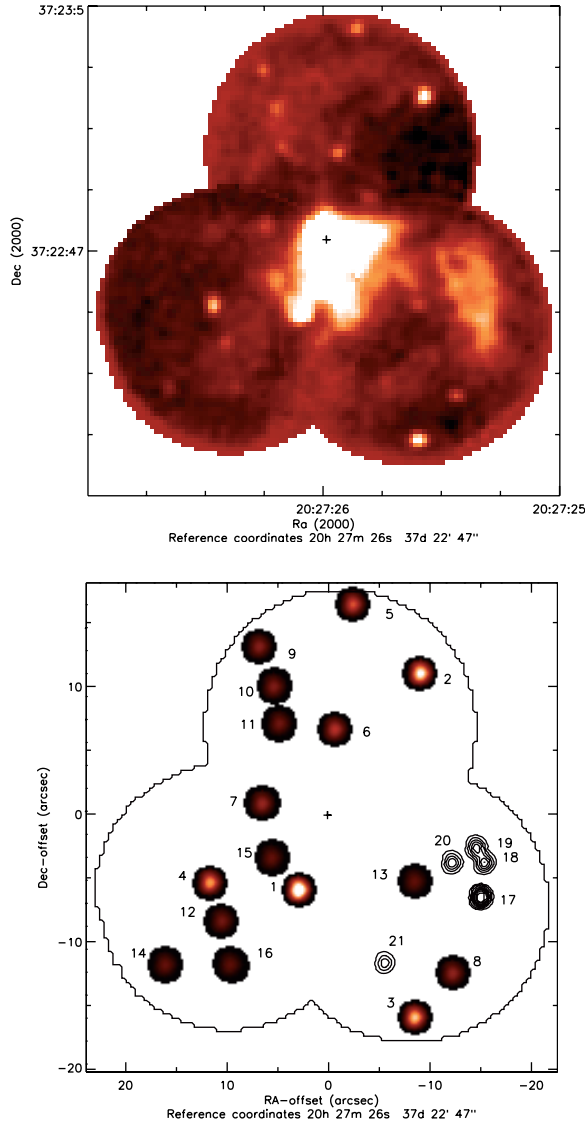


**Fig. 2.** *Up:* continuum emission at 2.1  $\mu\text{m}$ . *Low:* the stars labelled from 1 to 16 and the “star-like objects” (contours from 17 to 21, see text) found after extraction by *StarFinder*. The cross marks the position of S106 IR.

## 4. Results

### 4.1. The continuum emission at 2.1 $\mu\text{m}$

The Fig. 2 map exhibits a diffuse continuum all over the field with noticeable bright and dark regions. At 2.1  $\mu\text{m}$  this flux can come from the combination of several sources: diffusion of stellar light, in particular from S106 IR, emission of very small grains (An & Sellgren 2003), and free-bound emission from the ionized gas. A fan-shape extension to the southwest of the massive star is likely due to diffused stellar light. This feature was previously reported by Persson et al. (1988) on CCD images as two diffuse wisps. Other bright extended regions are present to the west of S106 IR, and to a lesser extent to the north and south. They can also be seen in the *JHK* images of Aspin et al. (1990). A dark lane is noticeable to the north of S106 IR, also mentioned by Smith et al. (2001). It is more obvious in Fig. 1. It opens slightly to the east and more to the west of the

**Table 1.** Positions and photometry at 2.1  $\mu\text{m}$  of stars close to S106 IR listed by order of decreasing brightness.

Star	$\Delta x^a$	$\Delta y^b$	Flux <sup>c</sup>	$K_{2.1}^d$
IR	0.0	0.0	23 600	5.9
1	2.1	−5.6	106.3	11.8
2	−7.2	11.0	80.9	12.1
3	−6.8	−15.6	65.8	12.3
4	9.1	−5.2	56.3	12.5
5	−2.1	16.4	41.1	12.8
6	−0.6	6.7	33.7	13.0
7	5.1	0.9	25.9	13.3
8	−9.8	−12.2	24.0	13.4
9	5.2	13.2	22.0	13.5
10	4.1	9.9	20.1	13.6
11	3.8	7.4	19.1	13.6
12	8.0	−8.1	17.4	13.7
13	−6.8	−5.2	14.6	13.9
14	12.5	−11.7	14.3	13.9
15	4.1	−3.4	14.0	14.0
16	7.4	−11.3	13.2	14.0
<i>Star-like objects</i>				
17	−11.8	−6.3	43.9	12.7
18	−12.2	−3.8	23.7	13.4
19	−11.5	−2.7	22.8	13.4
20	−9.6	−3.8	19.4	13.6
21	−4.3	−11.3	14.9	13.9

<sup>a</sup>  $\Delta x \cos \delta$  ("); <sup>b</sup>  $\Delta y$  (") relative to S106 IR; <sup>c</sup> in  $10^{-18} \text{ W m}^{-2}$ ; <sup>d</sup> magnitude at 2.1  $\mu\text{m}$ .

massive object. It will be interpreted below within the model of the nebula (Sect. 6.3).

### 4.2. Star photometry

From the Fig. 2 continuum map we were able to detect sixteen point sources identified as stars, with a contrast between 1.5 and 9. In addition, *StarFinder* detected five sources in regions where scattered light is greater (contrast < 1.5). As these sources could be merely density knots, they have been labelled “star-like objects”. The positions relative to S106 IR and the  $K_{2.1}$  magnitudes are given in Table 1. Only for a few sources has the infrared photometry been published by Aspin et al. (1990), to which we note large differences. They report 6.4 in  $K$  for S106 IR in a 3" aperture where we estimate a magnitude of 5.9 in the same aperture. The brightest star of the region after S106 IR, S106 IRS2, is out of our field, but the other bright stars, #2 and #4 in our list, are coincident respectively with S106 POS V and with S106 POS VI for which they report a  $K_{\text{mag}}$  of 10.7 while we derived 12.1 and 12.5. We expected a better comparison with the Two Mass All Sky Survey (2MASS) knowing that its limit in  $K_s$  mag is comparable to our observations. Within a radius of 20" centered on S106 IR a list of 30 stars (including the central star) was extracted. However, by

comparing this to our detection we obtained an acceptable coincidence in position (better than  $1''$  in each coordinate), except for S106 IR, for only 6 stars. In addition, except for S106 IR for which we agree, the  $K_s$  mags for these stars are all too bright by several magnitudes (up to 4). From their reported magnitudes we should have detected the other twenty stars. Therefore, we have chosen not report the few sources for which the positions agree our detection. This large discrepancy is consistent with the flag in the 2MASS data indicating upper limits for most values. It likely comes from the effect of source confusion in aperture photometry and from the clumpy, diffuse background emission which is not subtracted, as it is done in our measurements. Obviously, the detections are unreliable in such an embedded region. Hence, we report for the first time accurate stellar detections in the central region of S106. However, the “star-like objects” require higher spatial resolution to be confirmed.

### 4.3. Star population

The last census of stars in S106 is by Hodapp & Rayner (1991). From data in  $K$ -band imagery, they extracted 160 stars forming a 0.3 pc radius cluster centered approximately  $30''$  west and  $15''$  north of S106 IR. They reported stellar density as high as 1500 stars per projected  $\text{pc}^2$  within the cluster, with the background stars accounting for approximately 150 stars per  $\text{pc}^2$ . Within our field of view of  $r \approx 0.12$  pc, two background stars are expected to be present. The 16 stars we detect in the continuum (Fig. 2) correspond to a star density of  $\sim 1400$  stars per  $\text{pc}^2$ . This number is consistent with the work of Hodapp & Rayner (1991), as could be expected since the completeness limit of magnitude is  $K = 14$  in both studies. Images obtained in  $JHK'$  with CISCO at Subaru (Fig. 1) and in  $HK_s$  with NIRSPEC at Keck II<sup>2</sup> reveal a larger number of sources ( $\approx 30$  sources) in the area covered by our field of view. These images combining the images in the  $H$  band have a better contrast for young star detection than only  $K$ -band images since these stars are blue objects. Taken with 8 m-class telescopes these images go deeper than any previous imaging, and can detect more sources given that the brightness function of the S106 cluster peaks at  $K = 14.5$  and falls to zero at  $K = 17.5$  (Rayner 1994).

For the stars we detected (Table 1) we have tried to constrain the stellar masses in order to characterize the star population in this region. If one considers a mean visual extinction of  $A_V \approx 12.5$ , as derived by Felli et al. (1985) and Hodapp & Rayner (1991), and using the relation  $A_K = 0.112 A_V$  from Rieke & Lebofsky (1985) one can derive a typical extinction of  $A_K = 1.4$ . Taking the distance of 1.2 kpc (Rayner 1994) and assuming a coeval formation for S106 IR and the star cluster, we can adopt an age of a few  $10^5$  years (Hodapp & Rayner 1991), which means that these stars must be considered as pre-main sequence (PMS) stars. A model of the mass of a PMS star as a function of  $M_K$  for a given age has been developed by Zinnecker et al. (1993). From the  $3 \times 10^5$  years curve the derived masses of the stars around S106 IR are listed in Table 2 showing that a dozen out of the 16 sources are of sub-solar

**Table 2.** Absolute  $K$  magnitude ( $M_K$ ) and mass of the stars close to S106 IR (Fig. 2) estimated for an age of  $3 \times 10^5$  yr and a distance of 1.2 kpc (see text).

Star	$M_K$	Mass (in $M_\odot$ )
1	0.0	2.0
2	0.3	1.4
3	0.5	1.2
4	0.7	1.0
5	1.0	0.8
6	1.2	0.6
7	1.5	0.5
8	1.6	0.5
9	1.7	0.4
10	1.8	0.4
11	1.8	0.4
12	1.9	0.4
13	2.1	0.4
14	2.1	0.4
15	2.2	0.4
16	2.2	0.4

mass. Hence, our limit of  $K \approx 14$  prevents the detection of lower masses. Assuming that we identified in our field all the stars down to  $K = 14$  we can conclude that most of the extra sources seen in the deeper images are of lower mass. Extended to the full cluster it would mean that about half of the S106 star cluster population is of mass  $< 0.4 M_\odot$ . This value is consistent with the conclusion of Rayner (1994) that the Initial Mass Function flattens out in the range 0.5 to  $0.1 M_\odot$ . However, the minimum mass of Table 2 is based on several assumptions. First, the distance of S106 has a direct incidence on this limit. We adopted the revised distance which appears more accurate than previous estimates. With the distance of 600 pc commonly used (Staude et al. 1982) the mass limit of Table 2 would be lower, equal to  $0.15 M_\odot$ . In addition, the visual extinction is far from uniform over the field. However, as indicated in the table, a change of 0.5 in absolute  $K$  magnitude, which corresponds to about 5 in visual magnitude, which is the range of variation of  $A_V$  (Felli et al. 1985), does not significantly change the mass. The age estimate is also questionable. If an older age for the star cluster is considered, for example  $7 \times 10^5$  yr, the mass limit of the sample becomes  $0.75 M_\odot$ . However, models reproduce the S106 luminosity function for a much younger age (Zinnecker et al. 1993). Hence, S106 as a site where mainly sub-solar mass stars formed seems the most robust conclusion that can be drawn. Therefore, this cluster might be a good place to search for brown dwarfs.

### 4.4. Intensity map of the $H_2$ 1–0 $S(1)$ emission line

#### Bright regions

From Fig. 3a we see regions of bright  $H_2$  emission located to the north, southeast and southwest of S106 IR that have

<sup>2</sup> <http://www.astro.ucla.edu/irlab/nirspec/s106.html>

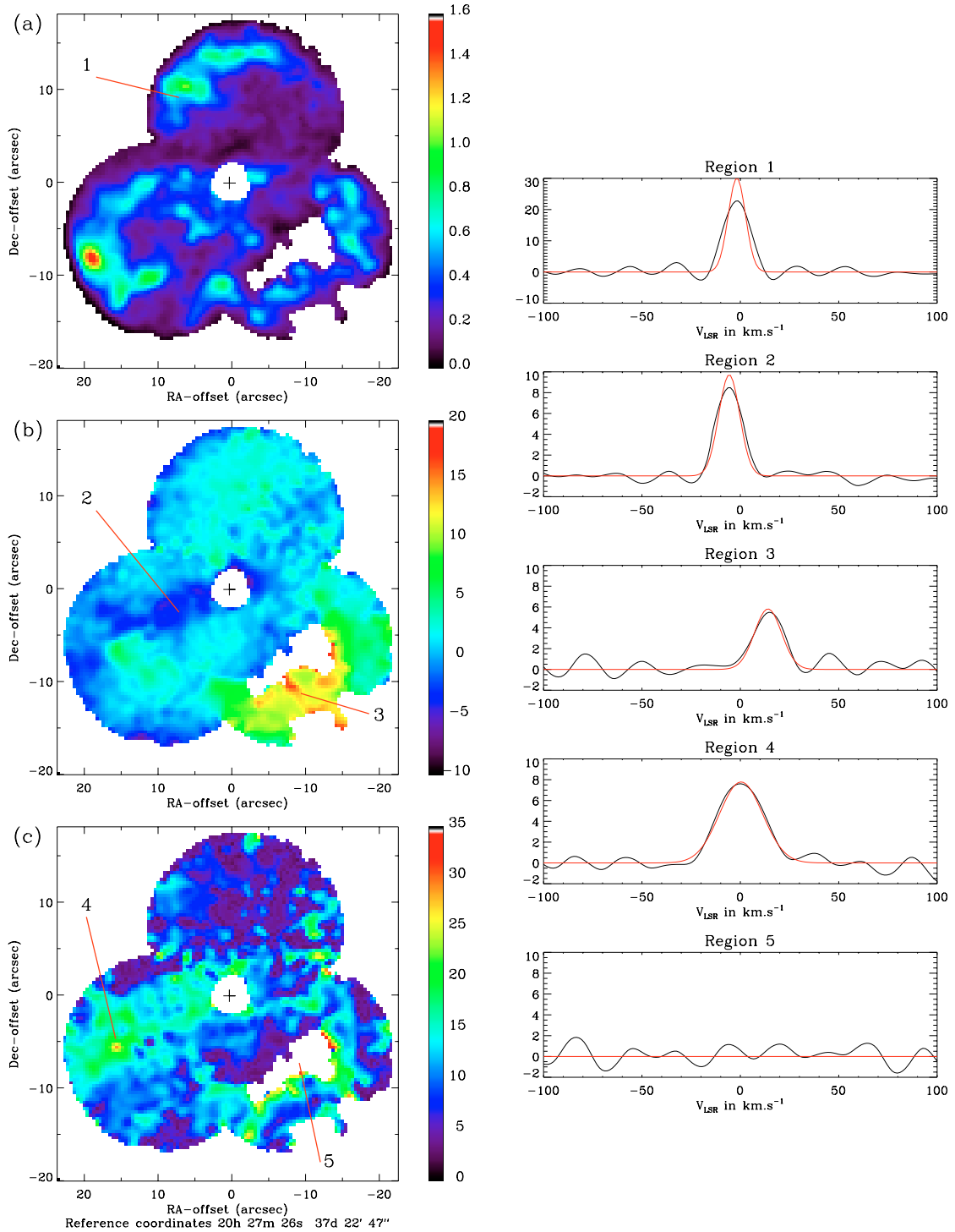


**Fig. 3.** The  $\text{H}_2$  1–0  $S(1)$  line in S106. The central cross marks the position of S106 IR. **a)** Computed integrated intensity map in  $10^{-18} \text{ W m}^{-2}/\text{pixel}$ ; **b)** LSR velocity map (in  $\text{km s}^{-1}$ ); **c)** linewidth ( $FWHM$ ) map (in  $\text{km s}^{-1}$ ). On the right column, 5 line profiles extracted at the positions marked by number on the maps. *From top to bottom:* # 1 at the mean velocity of the gas; # 2 in the “blue lane”; # 3 in the region of positive velocity; # 4 a remarkable star-like spot with  $FWHM = 30 \text{ km s}^{-1}$ ; # 5 in the “hole”. The Gaussian profiles from the deconvolution by the ILS are superimposed to the observed profiles.

elongated arc-shaped structures. They appear to be composed of clumps connected by a more diffuse gas, characterized by a factor of variation in intensity of more than 15 between the brightest and the lowest emission regions. From the larger field

map of Hayashi et al. (1990) our observation covers most of the intense  $\text{H}_2$  emission except to the north where the emission is more extended. These bright emission features are studied in detail in Sects. 5.1.1 and 5.3.

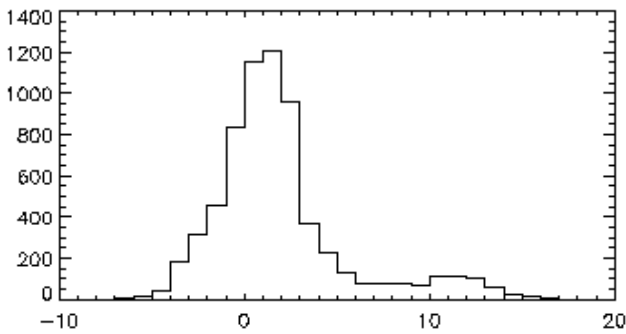


**Fig. 4.** Histogram in  $v_{\text{LSR}}$  of the  $\text{H}_2$  1–0  $S(1)$  line centers in the field around S106 IR made by bins of  $1 \text{ km s}^{-1}$ . X-axis:  $v_{\text{LSR}}$  in  $\text{km s}^{-1}$ ; y-axis: number of pixels.

#### Low-emission regions: the “dark lane” and the “hole”

The low emission fills the field with two remarkable structures, also observed in the continuum map (Fig. 2-up): i) an E-W “dark lane” to the north of S106 IR; ii) a region with a rectangular shape to the south of S106 IR where no  $\text{H}_2$  emission is detected at more than  $3\sigma$  rms. It is referred to as the “hole”.

#### 4.5. Velocity, linewidth maps of the $\text{H}_2$ 1–0 $S(1)$ line

The molecular gas has a rather uniform velocity as seen in the velocity map (Fig. 3b), with no flow structure, more typical of a turbulent gas. From the histogram of the velocity line centers (Fig. 4) the peak of the distribution is at  $v_{\text{LSR}} \approx +1.5 \text{ km s}^{-1}$  with a maximum dispersion of  $\pm 7 \text{ km s}^{-1}$ . The extended red wing with a maximum velocity of  $+15 \text{ km s}^{-1}$  corresponds to a specific region located just below the “hole”. Note that the mean  $\text{H}_2$  velocity is slightly different from the mm CO velocity reported by various authors (Loushin et al. 1990; Little et al. 1995; Schneider et al. 2002) which is  $v_{\text{LSR}} = -1.3 \text{ km s}^{-1}$ .

A lane of approaching material with respect to the main gas velocity (hereafter labelled “blue lane”) at  $-3 \text{ km s}^{-1}$  (profile #2 in Fig. 3b), stretched eastward through S106 IR, appears clearly in the velocity map. It corresponds to a region of  $\sim 15 \text{ km s}^{-1}$  linewidth on the linewidth map (Fig. 3c). This map shows a background with linewidths typically of  $\sim 10 \text{ km s}^{-1}$  or less. This value is confirmed by non-fully resolved line profiles at the resolution of the data as shown by profile #1 in Fig. 3a. Note that there is no correlation between the intensity map (Fig. 3a) and the linewidth map meaning that the clumpy structure seen in intensity does not correspond to regions with broader lines. The analysis of the  $\text{H}_2$  linewidths is done in Sect. 5.1.3. A few compact areas locally show a very broad linewidth, like spot #4. They are studied in Sect. 5.4.

#### 4.6. The Brackett $\gamma$ line

Unlike the  $\text{H}_2$  lines the Bry lines cover a total velocity range of  $\sim 200 \text{ km s}^{-1}$ . The line profile at each point looks multiple which justified applying a multi-component analysis (Sect. 3.2.2) from which four velocity structures could be identified. Their respective range of velocity is given by the histogram in Fig. 5.

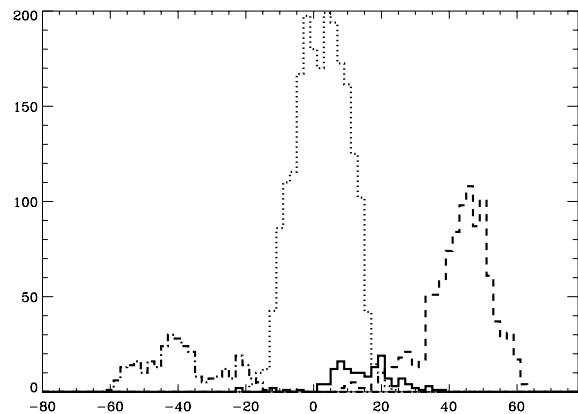


**Fig. 5.** Histogram in  $v_{\text{LSR}}$  of the Bry line center components in the field around S106 IR, made by bins of  $1 \text{ km s}^{-1}$ . X-axis:  $v_{\text{LSR}}$  in  $\text{km s}^{-1}$ ; y-axis: number of pixels. “Main” component (dotted, scaled down by a factor 2), “blue” (dash-dotted), “red1” (solid), “red2” high positive velocity component (dashed).

##### 4.6.1. Main component

The most important gas structure is called the “main” component. Its velocity ranges from  $-20$  to  $+20 \text{ km s}^{-1}$  in the histogram (Fig. 5), making it not possible to distinguish a north and a south lobe in the velocity map (Fig. 6b). A single structure is seen extending to the north and south of S106 IR with areas of positive and negative velocities in both sides. The map in integrated intensity (Fig. 6a) shows bright arc-shaped zones, in particular to the south of the “hole”, seen approximately at the same position on the  $\text{H}_2$  integrated map (Fig. 3a). The prominent region in the intensity map to the southwest of S106 IR is studied in more detail in Sect. 5.2. The northern bright area is cut by the edge of the field. It appears more extended on the map of Hayashi et al. (1990) and of Feldt et al. (2002). The E-W “dark lane” to the north of S106 IR, mentioned in the  $\text{H}_2$  intensity map, (Fig. 3a) is also seen as a region of weak Bry emission.

Except in the “dark lane” where it can be due to two components not separated in weak line profiles, the linewidths shown on the Fig. 6c map are homogeneous over the field, with a mean value of  $33 \text{ km s}^{-1}$ . This would correspond to a temperature of  $\sim 24\,000 \text{ K}$  if the emission were purely thermally broadened.

##### 4.6.2. The “blue”, “red1” and “red2” components

A positive velocity component with a velocity as high as  $60 \text{ km s}^{-1}$  is detected in two separate lobes, one to the north and the other to the south of S106 IR. Is it physically a single structure or two? Due to the common positive velocity this component is called “red2”. The structure is easily resolved because of its velocity range,  $[30\text{--}60] \text{ km s}^{-1}$ , well separated from the “main” component. However, its line intensity is weaker than in the “main” component, roughly by a factor of 3, except in the region of the “hole” (shown in contour in Fig. 7a) indicating that its emission is likely partly absorbed by the forefront material.

Two more structures are detected only to the south, one with a negative velocity (“blue”), the other one with a positive

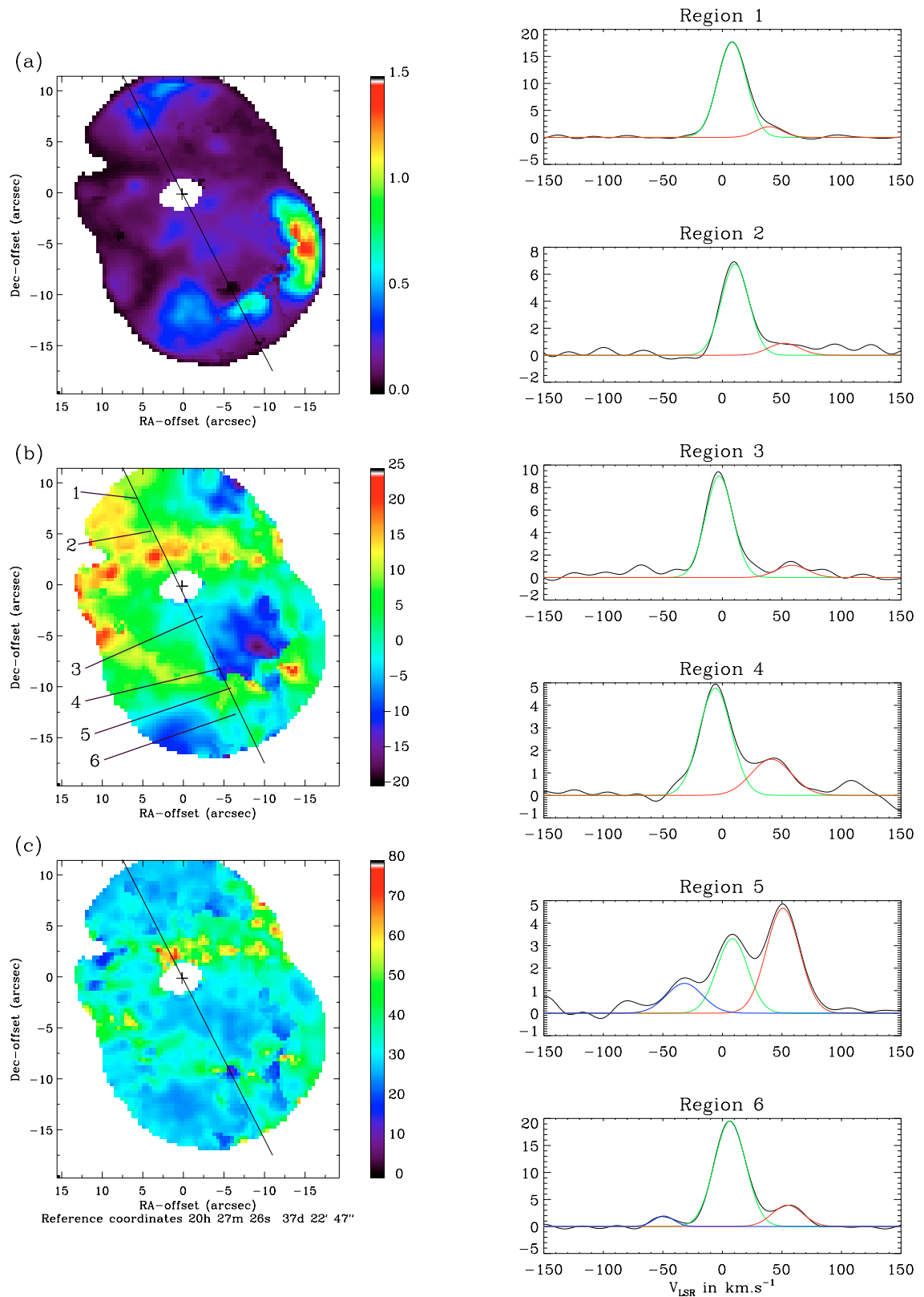


**Fig. 6.** Bry “main” component. **a)** Integrated intensity in  $10^{-17}$  W m<sup>-2</sup>/pixel; **b)** LSR velocity map of the line centers (color scale in km s<sup>-1</sup>); **c)** linewidths map (*FWHM*) in km s<sup>-1</sup>. On the right column, line profiles taken along the main axis of the H II region through S106 IR (cross), with their fitted components.

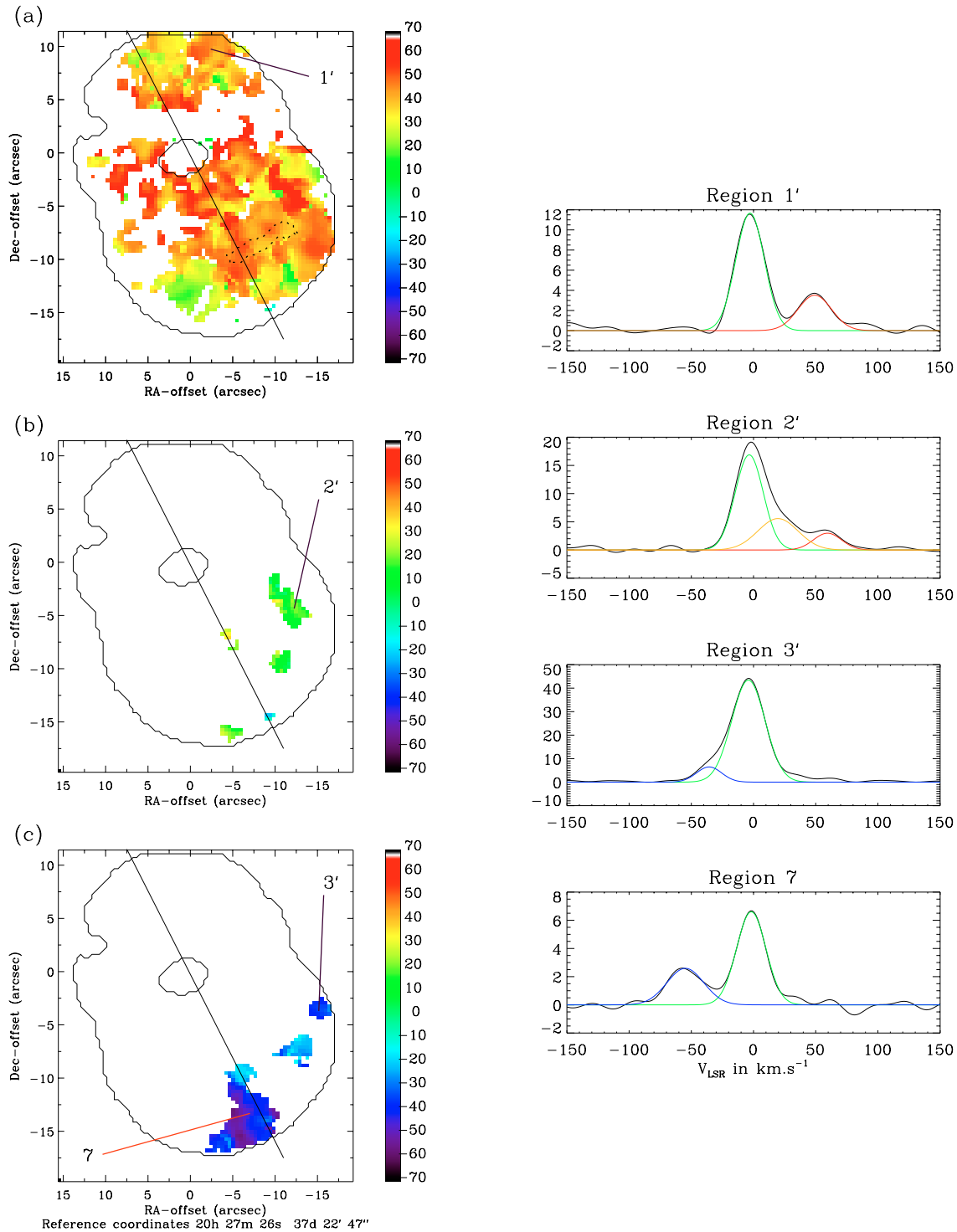


**Fig. 7.** LSR velocity maps of the three Bry structures other than “main” (color scales in  $\text{km s}^{-1}$ ). **a)** “red2” – the dashed contour indicates the position of the “hole” where this component is more intense than the “main” component (see profile #5 in Fig. 6); **b)** “red1”; **c)** “blue”. On the right column, line profiles with their fitted components on the line of sight of each structure, at the positions marked by number.

velocity (“red1”). The location of these structures from the multi-component analysis is presented in Figs. 7b and 7c. They appear isolated only in a few patches. From a direct examination of the Bry line cube with the cube viewer at  $-40 \text{ km s}^{-1}$ , the peak of distribution of the “blue” component (Fig. 5), two long filaments are seen extending from S106 IR to each

side of the “hole”. They include the areas seen in Fig. 7c that are the brightest parts of a more extended structure, difficult to fully extract by automatic line decomposition. Similarly, the “red1” structure is not completely visible because of its range of velocity overlapping the “main” and the “red2” components.

## 5. Excitation conditions in the environment of S106 IR

### 5.1. The $H_2$ line intensity and the ratio map

On the  $H_2$   $1-0S(1)/2-1S(1)$  line ratio map shown in Fig. 8 (upper panel) low values are found for the diffuse gas and higher values up to 9 for the emission clumps. Low values (around 1–2) are indicative of pure fluorescence following UV-pumping, whereas larger values show a contribution from collisions (Black & Van Dishoeck 1987). The highest theoretical value of 10 is expected for shocks driven by stellar winds, but an enhanced ratio associated with high-intensity lines is also expected for dense Photodissociated Regions (PDR) (Burton et al. 1990; Draine & Bertoldi 1996). The main features of this map are analyzed below.

#### 5.1.1. The $H_2$ eastern flow

A noticeable feature in Figs. 3a and 8 (upper panel) is the bright  $H_2$  emission region in field 3, with a U-shape to the east of S106 IR. It is located at the end of the “blue lane” (Fig. 3b). It coincides with the maximum of the  $H_2$  ratio map, around 9, and with the region of broad linewidth (Fig. 3c). From previous studies (Hayashi et al. 1990; Joblin et al. 2000; Smith et al. 2001) the emission in the Bry line and in the PAH bands are weak or absent in this region. The diffuse continuum emission at  $2.1 \mu\text{m}$  (Fig. 2) is also noticeably weak. Thus, it is not a PDR. A possible explanation for this emission is that S106 IR has released a radial flow with a maximum intensity at a position angle of  $\text{PA} = 118^\circ \pm 2$ , almost in the plane of the sky, which is observed at a projected velocity of  $\sim -3 \text{ km s}^{-1}$ . This flow when propagating induces a shock in the ambient gas and generates additional turbulence and a wide bow-shock structure (Raga & Cabrit 1993).

#### 5.1.2. Detection of PDRs and PDR model

Values around 5–6 to the southwest of S106 IR suggest a dense PDR. Successive bright fronts are observed in Bry and  $H_2$  emission (Fig. 8-low), and also PAH emission (Joblin et al. 2000) revealing a PDR viewed edge-on. To the north of S106 IR, values between 7 and 8 are observed which also indicate PDRs with higher densities or an additional contribution from shocks. The continuum emission at  $2.1 \mu\text{m}$  (Fig. 2) also is intense. Thus, except for the vicinity of S106 IR dominated by scattered starlight, this continuum is very similar to the one present in several PDRs (Sellgren 1984) where its emission comes from very small grains excited by the absorption of single UV photons (Sellgren et al. 1992; An & Sellgren 2003).

To gain more information on the physical conditions of the PDRs associated with S106 IR, we ran the stationary, 1-D and plane-parallel PDR model of Le Bourlot et al. (1993)<sup>3</sup> in its most recent version (see also Le Petit et al. 2002). We computed the intensities of the  $H_2$  lines using the density  $n = n_{\text{H}} + 2n_{\text{H}_2}$  as a parameter. The UV radiation field impinging the cloud is calculated using the characteristics derived by

<sup>3</sup> Code available at <http://aristote.biophy.jussieu.fr/MIS>

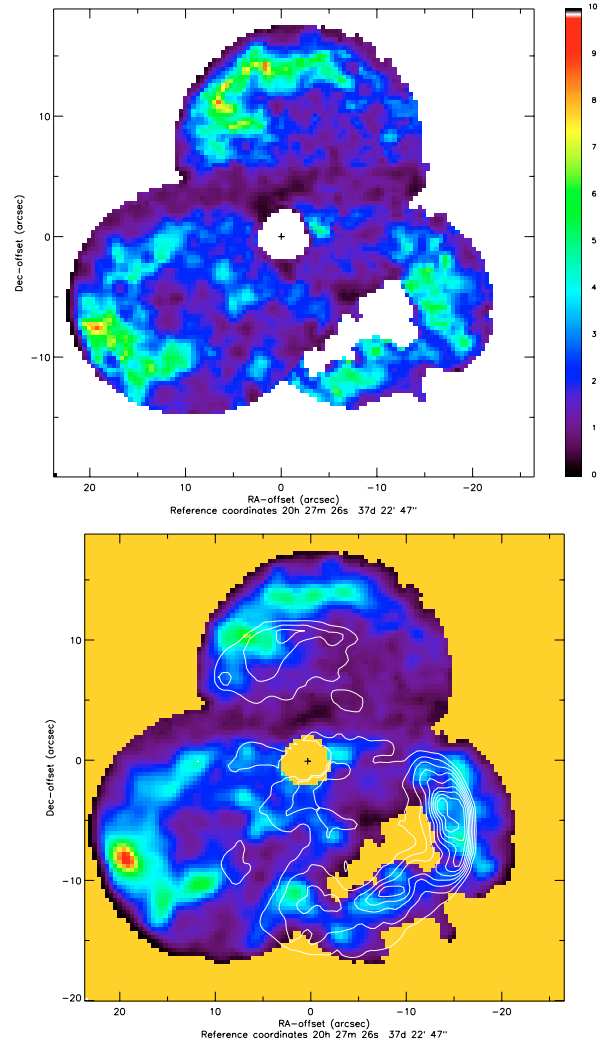


**Fig. 8.** *Up:*  $H_2$   $1-0S(1)/2-1S(1)$  line ratio. *Low:* contours of the Bry emission overlaid on the  $2.12 \mu\text{m}$   $H_2$  emission line.

Van den Ancker et al. (2000) on the star S106 IR, e.g. a temperature of 37 000 K and a luminosity of  $4.2 \times 10^4 L_{\odot}$ . We used a file from the Kurucz library (1993)<sup>4</sup> as a model for the spectrum of S106 IR. This led to a radius of  $17.2 R_{\odot}$  to fit the luminosity value. From the position of the bright southwest region in the continuum and in Bry (Figs. 2-up, 6a) the distance of the massive source to the molecular zone was taken equal to 0.090 pc (assuming a distance of 1.2 kpc for S106). The FUV field intensity incident on the PDR was found to be  $7.2 \times 10^5$  in units of  $G_0$  (Habing field). We can adjust the density so that the calculated values for the  $H_2$  line intensity match the observed ones. Both the  $1-0S(1)/2-1S(1)$  line ratio and the line absolute intensities can be used to constrain the density. The model provides values of 1.9, 2.8, 4.6, 5.6, 6.6 and 8.5 for the  $H_2$  line ratio for densities of 1.0, 2.0, 3.0, 3.5, 4.0 and  $5.0 \times 10^5 \text{ cm}^{-3}$  respectively. The line ratio is 5–6 in the clumps of the PDR, leading to a typical density of  $3.5 \times 10^5 \text{ cm}^{-3}$ . The computed intensity for the  $1-0S(1)$  line is found to be a few  $10^{-7} \text{ W m}^{-2} \text{ sr}^{-1}$  depending on the angle between the incident FUV field and the line of sight. The PDR model allow us to

<sup>4</sup> <http://www.stsci.edu/ftp/cdbs/cdbs2/grid/k93models>

consider angles between 0 and  $45^\circ$  but not  $90^\circ$  (the case of an edge-on geometry). Since the line ratio was found to be insensitive to geometrical effects, it is a more accurate tracer of the density. However, we note that the 1–0  $S(1)$  line intensity is observed to be typically  $2\text{--}3 \times 10^{-7} \text{ W m}^{-2} \text{ sr}^{-1}$ , which is consistent with the computed value. For the more diffuse gas connecting the clumps, both the line ratio and the intensity of the lines can be explained by a density of  $10^5 \text{ cm}^{-3}$ . These results confirm previous estimates by Van den Ancker et al. (2000) who derived a density higher than  $\approx 10^5 \text{ cm}^{-3}$  in the PDR and a FUV radiation field  $G \geq 10^5 G_0$  from the intensity of atomic lines towards S106 IR, in particular the [Si II]  $34.8 \mu\text{m}$  line. Finally, the PDR model also solves the thermal balance and a gas temperature of 660 K is derived at the maximum of the  $\text{H}_2$  emission for a density of  $10^5 \text{ cm}^{-3}$  and 1240 K for  $n = 3.5 \times 10^5 \text{ cm}^{-3}$ .

### 5.1.3. Mean turbulence velocity

On the  $\text{H}_2$  linewidth map (Fig. 3c) most of the field shows a linewidth of  $\approx 10 \text{ km s}^{-1}$ , and higher values on the “blue lane” and on a few spots (Sect. 5.4). For a purely thermal broadening  $10 \text{ km s}^{-1}$  would correspond to a gas temperature of 4500 K. The derived temperatures from the model are significantly lower. Therefore, a mean turbulent velocity must be added to the thermal contribution. For the range of gas temperature which is considered (660 to 1240 K) a mean turbulence between  $6.3$  and  $5.9 \text{ km s}^{-1}$  is needed to reach  $10.0 \text{ km s}^{-1}$ , and between  $9.7$  and  $9.5 \text{ km s}^{-1}$  for an observed value of  $15 \text{ km s}^{-1}$ . The turbulent velocity can be compared to the sound speed value ( $c_s = \sqrt{\gamma kT/m_{\text{H}_2}}$ ) which gives  $c_s = 2.9 \text{ km s}^{-1}$  for  $T = 1240 \text{ K}$ . The molecular gas in the immediate environment of the massive star, traced by  $\text{H}_2$ , is largely dominated by supersonic turbulence.

### 5.2. Photoevaporating clumps in the southwest PDR

A full search of the data cubes led to the detection of three other atomic lines (Fig. 9a), at  $4733.82$ ,  $4619.79$  and  $4459.41 \text{ cm}^{-1}$  ( $2.1124$ ,  $2.1646$ ,  $2.2424 \mu\text{m}$ ), identified with the He I transitions 3P0–3S and 3F0–3G (first two lines) and a [Fe III] line (term 3H–3G). The associated emission is mainly localized in the region of the PDR to the southwest of S106 IR which is also bright in  $\text{Br}\gamma$  (Fig. 9c) and in the  $2.1 \mu\text{m}$  continuum (Fig. 2-up). The range of velocity where they are detected makes them part of the “blue” velocity component. Such lines have been detected for example in the ionized region of young PNe like NGC 7027 (Cox et al. 2002) for the helium lines and in the vicinity of the Galactic Center source GCIRS 13 (Lutz et al. 1993) for [Fe III]. They are typical of regions of very strong ionization radiation (e.g.  $16.2 \text{ eV}$  for [Fe III]). The  $22.92 \mu\text{m}$  line of [Fe III] was previously reported towards S106 IR by Van den Ancker et al. (2000) from an ISO spectrum.

Four point-like condensations are clearly seen when scanning the  $2.165 \mu\text{m}$  He I line line profile (Fig. 9b). They fall close to the edge given by the [Fe III] emission (Fig. 9a) which is tracing the presence of extreme UV photons from the

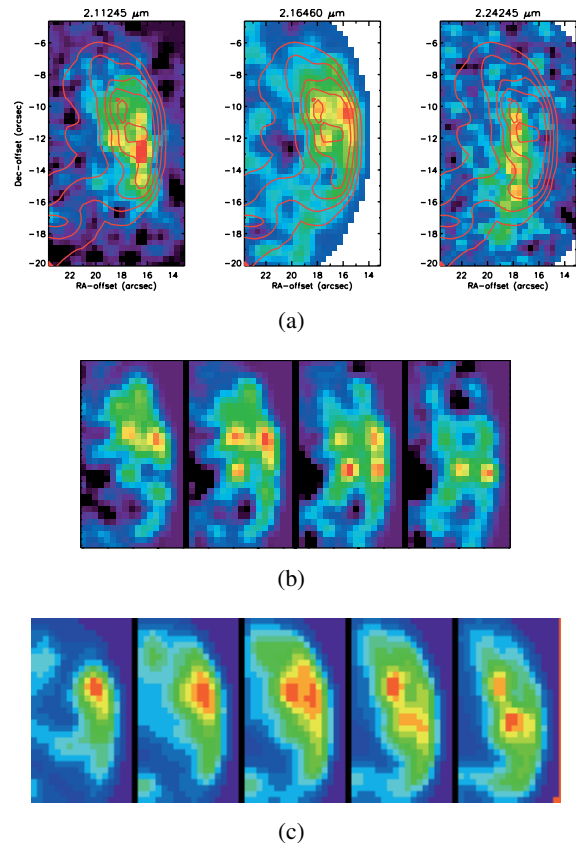


**Fig. 9.** Atomic lines in emission in the southwest PDR. **a)** From left to right, integrated intensity of line (central velocity):  $2.1124 \mu\text{m}$  He I ( $-19 \text{ km s}^{-1}$ ),  $2.1646 \mu\text{m}$  He I ( $-19 \text{ km s}^{-1}$ ) and  $2.2424 \mu\text{m}$  [Fe III] ( $-33 \text{ km s}^{-1}$ ); in contours, the  $\text{Br}\gamma$  line emission. The [Fe III] line comes from the innermost region of the PDR. **b)** Velocity channel maps (width:  $5 \text{ km s}^{-1}$ ) of the  $2.1646 \mu\text{m}$  He I line at central velocities from left to right of:  $-25$ ,  $-20$ ,  $-15$  and  $-10 \text{ km s}^{-1}$ . Four star-like clumps are clearly seen. **c)** Velocity channel maps (width:  $3 \text{ km s}^{-1}$ ) of the  $\text{Br}\gamma$  emission at central velocities from left to right of:  $-26$ ,  $-16$ ,  $-6$ ,  $+4$  and  $+12 \text{ km s}^{-1}$ .

massive star (Rodríguez 2002). A scan of the  $\text{Br}\gamma$  velocity channels (Fig. 9c) shows that more extended H recombination line emission is associated with the clumps, with a possible indication of a cometary shape with tails pointing away from S106 IR. As described by Gorti & Hollenbach (2002), the far-UV radiation induces an evaporative flow off the clump surface. This suggests that the  $2.165 \mu\text{m}$  He I line traces the surface of clumps whereas the  $\text{Br}\gamma$  line emission follows photoevaporating flows. Hence, these observations have to be explained by models of photoevaporating clumps in H II regions (Bertoldi 1989; Bertoldi & McKee 1990). The [2.165  $\mu\text{m}$  He I/ $\text{Br}\gamma$ ] line ratio has been studied by Lumsden et al. (2003) as a measure of the hardness of the UV field from the central star in the  $50.4\text{--}91.2 \text{ nm}$  range. For a star with  $T_{\text{eff}} \geq 37000 \text{ K}$  as estimated for S106 IR, this ratio is expected to be of about 0.04. We calculated this ratio for the condensations. A mean value of 0.033 was obtained which is consistent with the theoretical value. Rodríguez (2002) has studied Fe lines in H II regions and concluded that atomic iron arises from dust destruction by energetic photons. These condensations might be compared to

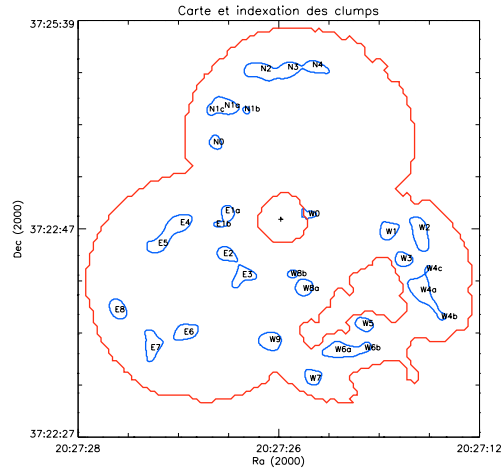


**Fig. 10.** Isocontour at 75% of the emission line peaks from Fig. 3 showing the clumpy structure of the warm H<sub>2</sub> gas.

the “Evaporating Gaseous Globules” (EGGs), well observed in the Eagle nebula M 16 by the Hubble Space Telescope (Hester et al. 1996), and of which McCaughrean & Andersen (2002) performed a near-IR imaging survey.

### 5.3. Clumps of H<sub>2</sub> emission

We have examined the structure of the H<sub>2</sub> emission by plotting the isocontours at 75% of maximum intensity. A structure of clump with an ellipsoidal shape appears, shown in Fig. 10 with a label for each clump. A major and minor axis were measured, perpendicular to one another. The clumps labelled E1b, N1c, W0, W4c and W8b on the figure were removed from the study because of their too small size. Without other constraints we set the third dimension of the clumps by using the average of the observed axes. We have seen that turbulence is important in the gas (Sect. 5.1.3). It is likely the process generating the observed clump structure. The mass was determined using a mean density of  $n_{\text{H}} = 3.5 \times 10^5 \text{ cm}^{-3}$ , as derived from the PDR model (Sect. 5.1.2). The mass range is found between a few  $10^{-4} M_{\odot}$  and a few  $10^{-3} M_{\odot}$  (Table 3).

A typical size of  $3.5 \times 10^{-3} \text{ pc}$  for the H<sub>2</sub> clumps and a density of  $3.5 \times 10^5 \text{ cm}^{-3}$  correspond to a depth of  $A_{\text{V}} = 2$ . Taking the typical example of the Orion Bar, the emission of the H<sub>2</sub> near-IR lines is observed over a depth of  $A_{\text{V}} \approx 1$  (Tielens et al. 1993) which corresponds to the zone in which the gas is hot and the destruction of H<sub>2</sub> is not too fast. Therefore, another possibility would be that the H<sub>2</sub> emission clumps are PDR shells of evaporating clumps exposed to a FUV field (Gorti & Hollenbach 2002). It is likely that these clumps will be destroyed before being overtaken by the ionization front of the advancing HII region. We indeed observe only four photo-evaporating clumps in the HII region which suggests that these are denser clumps emerging from the PDR.

### 5.4. Broad H<sub>2</sub> linewidth spots

The high-contrast point-like feature mentioned in Sect. 4.5 is seen in the linewidth map (spot #4 in Fig. 3c), to the

**Table 3.** Dimensions of the H<sub>2</sub> clumps identified in Fig. 10 for a distance of 1.2 kpc and computed masses obtained as discussed in Sect. 5.3 in the isodensity hypothesis with  $n = 3.5 \times 10^5 \text{ cm}^{-3}$ .  $d1$  and  $d2$  are the observed half main axes, and  $d3$  the half main axis perpendicular to the plane of the sky. Its value is taken as an average of the values of  $d1$  and  $d2$ .

Name	Dimensions <sup>a</sup> $10^{-3} \text{ pc}$				Mass $10^{-3} M_{\odot}$
	$d1$	$d2$	$d1/d2$	$d3$	
N0	4.09	4.31	0.95	4.20	2.66
N1a	3.66	5.94	0.62	4.80	3.75
N1b	2.51	2.68	0.94	2.60	0.59
N2	3.94	8.04	0.49	5.99	6.78
N3	3.20	5.61	0.57	4.40	1.61
N4	3.58	7.35	0.49	5.47	5.18
E1a	3.53	4.02	0.88	3.77	1.93
E2	2.98	4.66	0.64	3.82	1.91
E3	2.98	4.83	0.62	3.91	2.02
E4	3.21	6.33	0.51	4.77	3.48
E5	2.23	5.72	0.39	3.97	1.82
E6	3.83	6.93	0.55	5.38	5.14
E7	2.64	5.08	0.52	3.86	1.86
E8	3.93	5.69	0.69	4.42	3.55
W1	3.69	4.41	0.84	4.05	1.98
W2	3.95	9.27	0.43	6.61	8.67
W3	4.48	5.87	0.76	5.17	4.89
W4a	4.18	6.74	0.62	5.46	5.54
W4b	2.20	2.54	0.87	2.37	0.47
W5	3.21	4.73	0.68	3.97	2.17
W6a	3.90	9.24	0.42	6.57	8.52
W6b	2.34	3.44	0.68	2.89	0.84
W7	3.82	4.66	0.82	4.24	2.22
W8a	4.08	4.46	0.91	4.27	2.80
W8b	1.70	2.45	0.69	2.07	0.31
W9	4.52	5.71	0.79	5.11	4.76

<sup>a</sup> Half main axis.

southeast of S106 IR. No star continuum, no Bry emission counterpart and no enhancement of the H<sub>2</sub> emission are detected at this position. Apparently, there is no star present there. Only the 1–0 S(1) H<sub>2</sub> line is locally very broad. In this region the UV field is weak, as shown by the H<sub>2</sub> lines ratio (Fig. 8-up) and the absence of PAH emission (Joblin et al. 2000). Note that to the north of S106 IR in Fig. 3c there are several other spots of local H<sub>2</sub> line broadening, not as high as point #4, which have a linewidth of  $20 \text{ km s}^{-1}$  compared to  $\sim 10 \text{ km s}^{-1}$  in their vicinity. They are seen in regions of diffuse emission i.e. of low-density. What is the cause of these broad-line knots? This type of feature in a star-forming region is probably detected here for the first time, since a determination of the velocity field at high spectral resolution of such regions, as presented in this work, is not often obtained. As a plausible explanation, these velocity features might be vortices in a very turbulent gas observed in the close environment of S106 IR. Further studies at higher spatial resolution and in several H<sub>2</sub> lines are needed to better characterize these features and confirm their origin.

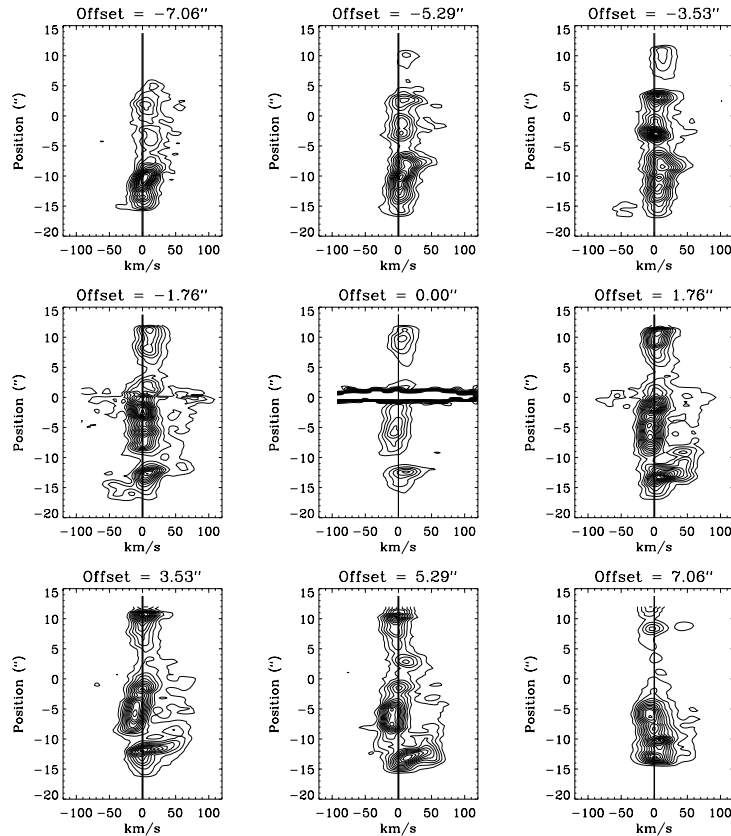


**Fig. 11.** Position-velocity Bry diagrams oriented according to the main axis of the H II region ( $PA = 30^\circ$ ) and taken at offset positions by  $1.76''$  steps east and west of S106 IR.

## 6. Dynamics of the ionized region

### 6.1. Bry position-velocity diagram

A position-velocity (PV) diagram has been built from the Bry data (Fig. 11), oriented according to the nebula axis, at  $PA = 30^\circ$ , determined from the  $JHK'$  image (Fig. 1) and the  $H\alpha$  line image (Bally et al. 1998). The presence of a “main” component centered at a near-zero LSR velocity in this direction is clearly seen in the diagram. Several authors have proposed that the lobes in S106 are indeed hollow cylinders (Smith et al. 2001, and references therein) made of two opposite flows. On the contrary, to explain the observations, the current geometry of the H II region is better described as a nebular cylinder mainly on the plane of the sky, filled with ionized gas to give this “main” velocity component. Only the dark lane just to the north of S106 IR gives the illusion of two separate lobes. Note that the layer of excited  $H_2$  which is at the periphery of the ionized region is centered on the same near-zero velocity (Fig. 4). With this geometry, limb-brightening effects must be seen on each side of the cylinder. Indeed, as studied in Sect. 5.1.2, a bright PDR seen edge-on, parallel to the nebula axis, is present to the southwest of S106 IR in the small field of the observations (Fig. 3a). From a wider field image in Bry (Hayashi et al. 1990) similar bright areas are seen on the opposite edge, which are likely other portions of PDRs seen edge-on.

### 6.2. Jets and accretion disk from S106 IR

Localized flows arising from the central object are present within the nebular cylinder, attested to in the PV Bry diagrams by panels with contours peaking at  $-50 \text{ km s}^{-1}$  and  $+50 \text{ km s}^{-1}$  and more, and by the identified velocity components called “red1”, “red2” and “blue”. For the fastest one (“red2”) a time scale of about 1400 yr can be determined assuming a distance reached of 0.1 pc and a true velocity of  $70 \text{ km s}^{-1}$ . It should be the most recent active event. The presence of jets in the environment of high-mass stars is predicted by the accretion theory in which the massive star forms in a scenario similar to low-mass stars, e.g. involving a disk-mediated accretion process. The jets are either attributed to the star-disk interaction (Shu et al. 1994) or to disk wind (Blandford & Payne 1982; Konigl & Pudritz 2000; Casse & Keppens 2002). The launch of outflow from a Keplerian disk can lead to wind speeds of  $\sim 200 \text{ km s}^{-1}$  as modelled by Drew et al. (1998) to explain the linewidth of the S106 IR stellar lines. That has been already proposed to fit the high-temperature first overtone band of CO at  $2.3 \mu\text{m}$  in emission (Chandler et al. 1993) detected towards S106 IR, as in other similar BN-type objects. In fact, the radio continuum imagery at 23 GHz with MERLIN (Hoare & Muxlow 1996) of S106 IR with a major axis at  $PA = 117^\circ \pm 2$  strongly suggests a disk-shape. This direction falls perpendicular to the axis of the nebula which is determined at  $PA = 30^\circ$  and matches exactly the eastern flow direction seen in  $H_2$

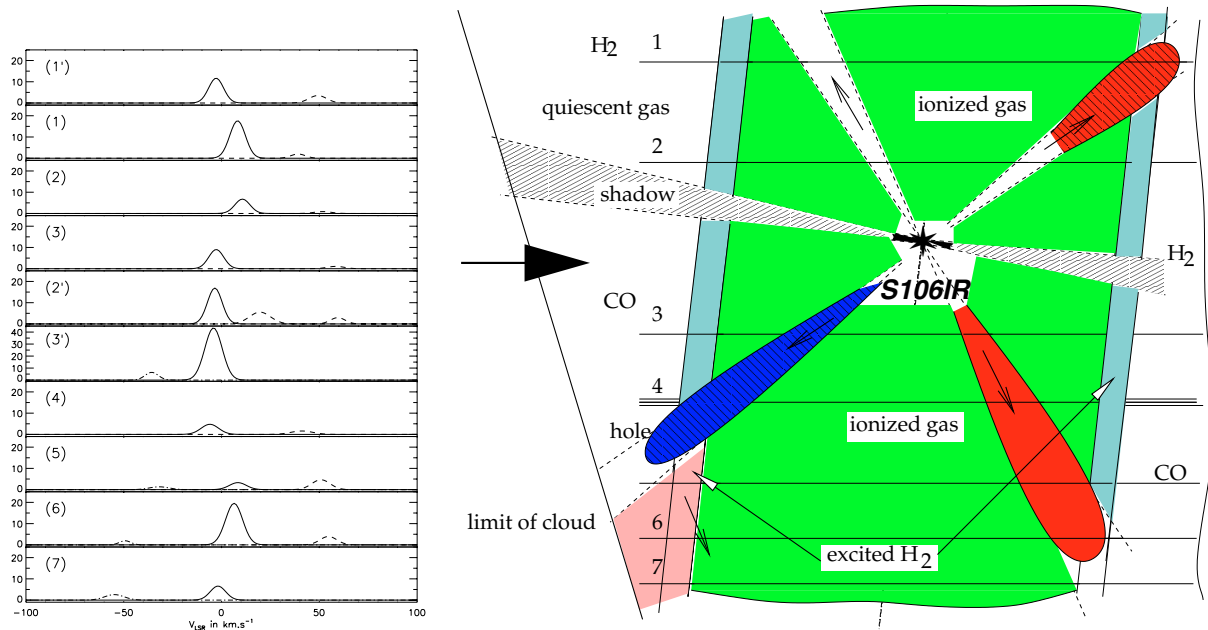


**Fig. 12.** Model of the S106 IR environment in the direction of the line of sight (arrow at left), in a plane containing the massive star and according to the main axis of the H II region. The horizontal lines from 1 to 7 refer to the Br $\gamma$  line components shown at right, extracted at the position numbers indicated in Figs. 6 and 7.

(Sect. 5.1.1). In addition, Persson et al. (1988) had proposed that the E-W “dark lane” observed in Br $\gamma$  and in H $_2$ , just to the north of S106 IR was a shadowing effect of a circumstellar disk preventing ionizing UV photons from reaching the gas in these regions. We adopt this hypothesis, also compatible with the fan-shape excess of diffuse light seen in the 2.1  $\mu\text{m}$  continuum map (Fig. 2) originating from S106 IR to the southwest of the massive star. All this strongly reinforces the idea of an active disk around S106 IR.

It is therefore likely that the jet/outflow events revealed by BEAR in Br $\gamma$  and in H $_2$  (eastern flow) are related to the activity of the disk, whether it is accretion, wind or photoevaporation by the central, massive star (Hollenbach et al. 1994). S106 IR is probably not an isolated case in this category since the presence of remnant accretion disks around several massive YSOs has been recently proposed (Bik et al. 2003). The formation of a massive protostar through an accretion disk was also shown in M 17 by Chini et al. (2004). Numerical simulations of disk wind reveal a structure with a dense, nearly-equatorial, low-velocity flow and a more polar, lower-density and higher velocity flow (Proga et al. 1998) which seems to fit with our observations. The simulations also predict that the total mass-loss rate depends only on the total luminosity of the star plus disk system whereas the geometry and time properties of the outflow depend on the geometry of the radiation field (Proga et al. 1999). This whole picture reinforces the idea that S106 IR formed through a scenario of accretion mediated by a disk. The main outflow has now stopped which shows that the star is reaching the main sequence. A remnant disk still present leads to active events attested to by the broad jets we have detected, which contribute to the turbulence of the surrounding molecular cloud.

### 6.3. A 3-D model of the environment of S106 IR

All the information discussed above has been used to be integrated into a new model of the immediate environment of S106 IR. Shown in Fig. 12, it presents a schematic cut through the thickness of the molecular cloud. For the sake of simplicity the limits between the molecular and the ionized gas are drawn as straight lines, which is not the case. The main elements entered in the model are the following:

1. A cylinder of ionized gas almost in the plane of the sky, excited by the UV flux from the massive source S106 IR. The cylinder should be expanding. To the north and south, regions of positive and negative velocity are observed in the “main” velocity structure of Br $\gamma$  (Fig. 6b). To the south of S106 IR the nebular cylinder is opening out of the molecular cloud, which appears clearly on the full scale image (Fig. 1). This is also compatible with the higher extinction observed to the north compared to the south. Thus, S106 IR is located near the edge of its parent molecular cloud.
2. An accretion disk around S106 IR creating a region of shadow in the ionized gas and in the molecular gas. The disk is slightly inclined relative to the line of sight in order to account for the northern location of the “dark lane” observed in H $_2$ . Its axis is coincident with the axis of the cylinder of ionized gas.
3. A pair of bipolar jets arising from the central source. The velocity structures, “blue” and “red2” with the same opposite velocity are interpreted as the components of two bipolar jets, the northern blue lobe of one of them being missing. The “red2” structure is detected to the north and south of S106 IR, but not the “blue” structure. For this reason, in Fig. 12 the region is represented as devoid of gas. The two red flows must have the same projected velocity of

$\approx 50 \text{ km s}^{-1}$  to explain the presence of the “red2” structure to the north and the south of S106 IR.

4. A layer of excited  $\text{H}_2$ , typical of a PDR, at the periphery of the nebular cylinder.
5. A “hole” in the forefront of the molecular cloud, to the south of S106 IR. This “hole” was created by one of the above jets. The gas has been swept out in this region. The rectangular shape is an imprint of the section of the flow. Its red counterpart (northern part of “red2”) should have a similar section. This shape indicates that the flows are not highly collimated in the direction of the line of sight (Figs. 7a and 11) or the stellar jets are precessing during their lifetime.
6. A region of positive velocity of  $\text{H}_2$  ( $\sim 12 \text{ km s}^{-1}$ ) to the south of the “hole”. The  $\text{H}_2$  linewidth is broad at the edge of the “hole” (Fig. 3). It is proposed that the expansion motion of the flow that made the “hole” is pushing the molecular gas into the ionized region.

All these elements clearly make S106 IR a typical example of a massive star near the end of its formation phase and S106 another example of a PDR.

## 7. Conclusions

The observation of the environment of the embedded, massive source S106 IR with BEAR has brought new results on the dynamics and the excitation conditions of the evolved H II region and the surrounding molecular cloud:

1. Members of the low-mass star cluster formed with S106 IR are detected in the central region and are mainly sub-solar low-mass stars.
2. Although the central object approaches the main sequence, it is still active as the source of two pairs of bipolar flows identified in the ionized gas, and an eastern flow in the molecular gas. The massive star is located in the middle of a nebular cylinder of about 0.1 pc in radius carved in the molecular gas.
3. PDR structures have been shown to exist at the limit of the cylinder. In one of them, to the southwest of S106 IR, emission lines of He I and [Fe III] are detected with several point-like photoevaporating clumps seen in helium, which may reveal externally ionized circumstellar material.
4. UV-absorption and shocks are participating in the excitation of the  $\text{H}_2$  molecular gas which probes the periphery of the H II region. The excited gas shows emission with a clumpy structure and an almost uniform velocity. It is the origin of supersonic turbulence ( $\geq 6 \text{ km s}^{-1}$ ), generating a few local vortices. The density in this gas layer varies from 1 for the regions of diffuse emission to  $3.5 \times 10^5 \text{ cm}^{-3}$  for the clumps. With this density the mass of the clumps is small, of the order of  $10^{-3} M_{\odot}$ .

These results must be replaced within the scenario described by Healy et al. (2004) of low-mass star formation in the environment of an H II region. Applied to S106, after a first phase of formation at the birth of the massive star S106 IR and of the current cluster of low-mass stars, it would predict a phase

of star formation which could be triggered by the expansion of the ionization front in the surrounding molecular gas. With the current data there is no indication of such a phase starting. The gas probed by the quadrupolar  $\text{H}_2$  lines at the periphery of the H II region, is hot, low-density gas. To probe whether dense molecular clumps are formed in the colder gas requires complementary sub-mm observations in HCN and  $\text{HCO}^+$  as made in the Orion Bar (Lis & Schilke 2003) at high spatial resolution. Early observations were conducted in  $\text{HCO}^+$  which detected a ring of dense molecular gas around S106 IR with an inner radius of almost the size reported here for the excited  $\text{H}_2$  cylinder (Loushin et al. 1990). More sensitive and higher resolution observations are required to conclude whether protostellar clumps are formed there which could collapse to form low-mass stars in advance of the ionization front.

More generally, this work illustrates how *IFS at high spectral resolution* is a powerful tool to study complex star-forming regions. The limitation of the current analysis is obviously the size of the available field with BEAR. Special procedures were developed to merge several cubes to increase the field coverage, but the study remained limited to the central region. An overview of the kinematics of the entire star-forming region, with the full extent of the UV-influenced gas, would need a field of several arcmins for a full appraisal of the interaction of S106 IR with its environment. The same comment applies to the study of most star-forming regions. This will have to await a new generation of instruments able to associate high spectral resolution ( $\leq 10 \text{ km s}^{-1}$ ) and a large field ( $\sim 10'$ ) in the infrared. Such characteristics are provided by the Imaging FTS as proposed in Maillard & Joblin (2004) which is missing in the instrumentation of modern telescopes.

*Acknowledgements.* We gratefully thank the referee, M. van den Ancker, whose comments stimulated a thorough revision of the paper. We acknowledge helpful discussions with J. Le Bourlot for the appropriate use of his PDR program.

## References

- An, J. H., & Sellgren, K. 2003, *ApJ*, 599, 312
- Aspin, C., Rayner, J. T., McLean, I. S., & Hayashi, S. S. 1990, *MNRAS*, 246, 565
- Bally, J., Yu, K. C., Rayner, J., & Zinnecker, H. 1998, *AJ*, 116, 1868
- Bertoldi, F. 1989, *ApJ*, 346, 735
- Bertoldi, F., & McKee, C. F. 1990, *ApJ*, 354, 529
- Bik, A., Kaper, L., Waters, R., et al. 2003, in *Star Formation at High Angular Resolution*, IAU Symp., 221, 12
- Black, J. H., & van Dishoeck, E. F. 1987, *ApJ*, 321, 412
- Blandford, R. D., & Payne, D. G. 1982, *MNRAS*, 199, 883
- Burton, M. G., Hollenbach, D. J., & Tielens, A. G. G. M. 1990, *ApJ*, 365, 620
- Casse, F., & Keppens, R. 2002, *ApJ*, 581, 988
- Chandler, C. J., Carlstrom, J. E., Scoville, N. Z., Dent, W. R. F., & Geballe, T. R. 1993, *ApJ*, 412, L71
- Chini, R., Hoffmeister, V., Kimeswenger, S., et al. 2004, *Nature*, 429, 155
- Cox, P., Huggins, P. J., Maillard, J. P., et al. 2002, *A&A*, 384, 616
- Diolaiti, E., Bendinelli, O., Bonaccini, D., et al. 2000, *A&AS*, 147, 335
- Draine, B. T., & Bertoldi, F. 1996, *ApJ*, 469, 269

- Drew, J. E., Proga, D., & Stone, J. M. 1998, *MNRAS*, 296, L6
- Eiroa, C., Elsässer, H., & Lahulla, J. F. 1979, *A&A*, 74, 89
- Feldt, M., Puga, E., Weiß, A. R., & Hippler, S. 2002, in *Hot Star Workshop III: The Earliest Stages of Massive Star Birth*, ed. P. A. Crowther, ASP Conf. Ser., 267, 367
- Felli, M., Staude, H. J., Reddmann, T., et al. 1984, *A&A*, 135, 261
- Felli, M., Simon, M., Fischer, J., & Hamann, F. 1985, *A&A*, 145, 305
- Garden, R. P., & Geballe, T. R. 1986, *MNRAS*, 220, 611
- Gehrz, R. D., Grasdalen, G. L., Castelaz, M., et al. 1982, *ApJ*, 254, 550
- Gorti, U., & Hollenbach, D. 2002, *ApJ*, 573, 215
- Hayashi, S. S., Hasegawa, T., Tanaka, M., et al. 1990, *ApJ*, 354, 242
- Healy, K. R., Hester, J. J., & Claussen, M. J. 2004, *ApJ*, 610, 835
- Hester, J. J., Scowen, P. A., Sankrit, R., et al. 1996, *AJ*, 111, 2349
- Hoare, M., & Muxlow, T. 1996, in *Radio emission from the stars and the sun*, ed. A. R. Taylor, & J. M. Paredes, ASP Conf. Ser., 93, 47
- Hollenbach, D., Johnstone, D., Lizano, S., & Shu, F. 1994, *ApJ*, 428, 654
- Hodapp, K. W., & Rayner, J. 1991, *AJ*, 102, 1108
- Joblin, C., Maillard, J. P., Vauglin, I., Pech, C., & Boissel, P. 2000, in *H<sub>2</sub> in Space*, ed. F. Combes, & G. Pineau des Forêts (Cambridge University Press), *Astroph. Ser.*, 107
- Konigl, A., & Pudritz, R. E. 2000, in *Protostars and Planets IV*, ed. V. Mannings, A. P. Boss, & S. S. Russell (Tucson: Univ. of Arizona Press), 759
- Kurucz, R. L. 1993, *ATLAS9 Stellar Atmosphere Programs*, Cambridge, Mass.: Smithsonian Astrophysical Observatory
- Le Bourlot, J., Pineau des Forêts, G., Roueff, E., & Flower, D. R. 1993, *A&A*, 267, L233
- Le Petit, F., Roueff, E., & Le Bourlot, J. 2002, *A&A*, 390, 369
- Lis, D. C., & Schilke, P. 2003, *ApJ*, 597, 145
- Little, L. T., Kelly, M. L., Habing, R. J., & Millar, T. J. 1995, *MNRAS*, 277, 307
- Loushin, R., Crutcher, R., & Bieging, J. H. 1990, *ApJ*, 362, 67
- Lumsden, S. L., Puxley, P. J., Hoare, M. G., Moore, T. J., & Ridge, N. A. 2003, *MNRAS*, 340, 799
- Lutz, D., Krabbe, A., & Genzel, R. 1993, *ApJ*, 418, 244
- Maillard, J. P. 1995, in *3D optical spectroscopic methods in astronomy*, ed. G. Comte, & M. Marcelin, ASP Conf. Ser., 71, 316
- Maillard, J. P. 2000, in *Imaging the Universe in 3D*, ed. W. van Breugel, & J. Bland-Hawthorn, ASP Conf. Ser., 195, 185
- Maillard, J. P., & Joblin, C. 2004, in *Dome C Astronomy/Astrophysics Meeting*, ed. M. Giard (EDP Sciences) EAS Publ. Ser., in press
- McCaughrean, M. J., & Andersen, M. 2002, *A&A*, 389, 513
- Oasa, Y. 2001, Ph.D. Thesis, Univ. of Tokyo
- Paumard, T., Maillard, J. P., & Morris, M. 2004, *A&A*, 426, 81
- Persson, S. E., McGregor, P. J., & Campbell, B. 1988, *ApJ*, 326, 339
- Proga, D., Stone, J. M., & Drew, J. E. 1998, *MNRAS*, 295, 595
- Proga, D., Stone, J. M., & Drew, J. E. 1999, *MNRAS*, 310, 476
- Raga, A., & Cabrit, S. 1993, *A&A*, 278, 267
- Rayner, J. 1994, in *Infrared Astronomy with Arrays: The next generation*, ed. I. S. McLean (Pub. Kluwer), 185
- Rieke, G. H., & Lebofsky, M. J. 1985, *ApJ*, 288, 618
- Rodríguez, M. 2002, *A&A*, 389, 556
- Schneider, N., Simon, R., Kramer, C., Stutzki, J., & Bontemps, S. 2002, *A&A*, 384, 225
- Schneider, N., Simon, R., Kramer, C., et al. 2003, *A&A*, 406, 915
- Sellgren, K. 1984, *ApJ*, 277, 623
- Sellgren, K., Werner, M. W., & Dinerstein, H. L. 1992, *ApJ*, 400, 238
- Shu, F., Najita, J., Ostriker, E., et al. 1994, *ApJ*, 429, 781
- Smith, N., Jones, T. J., Gehrz, R. D., et al. 2001, *AJ*, 121, 984
- Solf, J., & Carsenty, U. 1982, *A&A*, 113, 142
- Staude, H. J., Lenzen, R., Dyck, H. M., & Schmidt, G. D. 1982, *ApJ*, 255, 95
- Tielens, A. G. G. M., Meixner, M. M., van der Werf, P. P., et al. 1993, *Science*, 262, 86
- Van den Ancker, M. E., Tielens, A. G. G. M., & Weslins, P. R. 2000, *A&A*, 358, 1035
- Zinnecker, H., McCaughrean, M. J., & Wilking, B. A. 1993, in *Protostars and Planets III*, ed. E. H. Levy, & J. I. Lunine (U. of Arizona Press), 429